Thermal structure of Venusian nighttime mesosphere as observed by VIRTIS-Venus Express

D. Grassi,[1] A. Migliorini,[2] L. Montabone,[3] S. Lebonnois,[3] A. Cardesìn-Moinelo,[4] G. Piccioni,[2] P. Drossart,[5] and L. V. Zasova[6]

[1]   The mapping IR channel of the Visual and Infrared Thermal Imaging Spectrometer (VIRTIS-M) on board the Venus Express spacecraft observes the CO_2 band at 4.3 μm at a spectral resolution adequate to retrieve the atmospheric temperature profiles in the 65–96 km altitude range. Observations acquired in the period June 2006 to July 2008 were used to derive average temperature fields as a function of latitude, subsolar longitude (i.e., local time, LT), and pressure. Coverage presented here is limited to the nighttime because of the adverse effects of daytime non-LTE emission on the retrieval procedure and to southernmost latitudes because of the orientation of the Venus-Express orbit. Maps of air temperature variability are also presented as the standard deviation of the population included in each averaging bin. At the 100 mbar level (about 65 km above the reference surface), temperatures tend to decrease from the evening to the morning side despite a local maximum observed around 20–21LT. The cold collar is evident around 65S, with a minimum temperature at 3LT. Moving to higher altitudes, local time trends become less evident at 12.6 mbar (about 75 km) where the temperature monotonically increases from middle latitudes to the southern pole. Nonetheless, at this pressure level, two weaker local time temperature minima are observed at 23LT and 2LT equatorward of 60S. Local time trends in temperature reverse about 85 km, where the morning side is the warmer. The variability at the 100 mbar level is maximum around 80S and stronger toward the morning side. Moving to higher altitudes, the morning side always shows the stronger variability. Southward of 60S, standard deviation presents minimum values around 12.6 mbar for all the local times.

Citation: Grassi, D., A. Migliorini, L. Montabone, S. Lebonnois, A. Cardesìn-Moinelo, G. Piccioni, P. Drossart, and L. V. Zasova (2010), Thermal structure of Venusian nighttime mesosphere as observed by VIRTIS-Venus Express, *J. Geophys. Res.*, *115*, E09007, doi:10.1029/2009JE003553.

1. Introduction

[2]   Air temperatures are among the most important experimental constraints in the study of planetary atmospheres. Most dynamical phenomena have clear counterparts in the temperature fields, while temperatures themselves drive a number of processes (namely, aerosol condensation and chemical stability of gaseous components) that affect the atmospheric energy budget. Temperatures in the Venus atmosphere have been investigated in detail by several entry probes that returned accurate profiles at very high vertical resolution and in a wide range of altitudes (cf. *Seiff* [1983] for an extensive review).

[3]   Probe measurements are however adversely affected by the sparsity of sampling. Consequently, remotely sensed measurements by orbiting spacecraft have been more effective in providing a general picture of Venus temperature fields. This class of data includes - among others - results from radio occultations [*Kliore*, 1985; *Yakovlev et al.*, 1991; *Jenkins et al.*, 1994; *Tellmann et al.*, 2009], stellar occultations [*Bertaux et al.*, 2007] and infrared radiometry/ spectroscopy [*Taylor et al.*, 1980; *Zasova et al.*, 2007].

[4]   Infrared observations take advantage of the variability of CO_2 opacity with wavelength in order to retrieve, by inversion, the temperature profile from the gas thermal emission. Since the technique exploits the ubiquitous atmospheric emission, large regions can be readily mapped. Consequently, infrared spectroscopy, despite a vertical resolution and a retrieval error worser than other remote sensing methods, has a relevant statistical value to build spatially extensive data sets.

[1]IFSI, INAF, Rome, Italy.
[2]IASF, INAF, Rome, Italy.
[3]Laboratoire de Météorologie Dynamique, IPSL, Université Pierre et Marie Curie, CNRS, Paris, France.
[4]ESA, INSA, ESAC, Villanueva de la Cañada, Spain.
[5]LESIA, Observatoire de Paris, Meudon, France.
[6]IKI RAS, Moscow, Russia.

[5] The Venus Express mission carries a variety of experiments suitable for the study of Venus temperature fields [*Titov et al.*, 2009; *Drossart et al.*, 2007]. In this context, the mapping IR channel of the Visual and Infrared Thermal Imaging Spectrometer (VIRTIS) is particularly interesting for its capability to return synoptic maps of temperatures in the indicative range 65–95 km [*Grassi et al.*, 2008]. In this paper we provide a short reminder of the retrieval method developed for VIRTIS and related performances, followed by a report on the current status of data set processing (section 2). Available temperature profiles were used to compute average thermal fields as a function of latitude, subsolar longitude (i.e.: local time) and pressure (section 3). Derived maps of air temperature mean values and standard deviations are presented, and compared with previous observations of the FTS on Venera 15 (section 4). A qualitative interpretation of the results is attempted as introductory work for future systematic comparisons against the results of global circulation models (section 5).

2. VIRTIS Data Set

[6] The VIRTIS instrument on board the Venus Express mission consists of a set of different subsystems, with specific measuring capabilities. VIRTIS-H is a high resolution grating spectrometer operating in the range 3–5 μm, with a typical resolution and sampling step of 1.5 nm (variable along the range and with spectral order). VIRTIS-M is a spectro-imager, able to acquire a stack of monochromatic images (a so-called 'cube') that allow the reconstruction of the spectrum for each pixel. VIRTIS-M operates simultaneously in the visible and infrared part of the spectrum. The covered ranges are 0.28–1.1 and 1–5.1 μm, with sampling steps of 1.9 and 11 nm respectively. The VIRTIS-M and –H instantaneous fields-of-view (IFOV) are 0.25 × 0.25mrad (for an individual pixel) and 1.74 × 0.58 mrad, respectively. These values, together with the Venus Express orbital parameters, lead to a horizontal resolution for individual pixels of 16.5 × 16.5 and 115 × 38 km respectively, in the case of measurements acquired at the apocenter. A complete description of the instrument and its radiometric performances is given by *Piccioni et al.* [2007]. The noise equivalent radiance pertinent to each measurement depends on several factors such as the instrument temperature and exposure time. A value of $5 \cdot 10^{-4}$ erg/(sec. cm^2 ster. nm) at 4.3 μm can be considered as typical.

[7] *Grassi et al.* [2008] presented an algorithm for the study of the thermal state of the Venus atmosphere from VIRTIS-M IR data. The method uses as input the radiance observed in the 4.3 μm CO_2 band in a VIRTIS-M spatial pixel in order to determine – by numerical inversion – air temperatures on a fixed reference pressure grid (vertical coordinate). The authors provided a quantitative assessment of retrieval errors based on the statistical analysis of a series of test retrievals performed on simulated observations. Once individual pixels are averaged in 10 × 10 bins to increase the signal-to-noise ratio, the code returns the vertical air temperature profile in the bin with a total error <1K in the region between 70 and 2 mbar (respectively, 66 and 83 km above the reference surface), and <4K throughout the entire range 100–0.1 mbar (64–95 km). The finite width of the averaging kernels imposes an effective vertical resolution

for the retrieval on the order of 10 km. The uncertainty in the determination of the effective altitude of the main cloud deck is the major source of retrieval errors below 70 km. On the other hand, the low signal level at the center of the 4.3 μm band makes the retrievals above 85 km particularly prone to instrumental noise, residual calibration errors and approximations in radiative transfer modeling.

[8] The daytime signal in the 4.3 μm region is dominated by the CO_2 non-LTE emission. This contribution is not modeled by the forward code embedded in the retrieval procedures of *Grassi et al.* [2008]. This fact precludes the estimation of the pure thermal emission and the applicability of the method to daytime data. Limitations of the forward code (approximations in the subroutines for the evaluation of CO_2 transmittances and the treatment of scattering) set also a maximum value for emission angles ($\varepsilon < \sim30°$) of data to be processed.

[9] The method by *Grassi et al.* [2008] has been routinely applied to the analysis of VIRTIS-M data. This paper presents results derived from this retrieval code. Due to limitations in available computing facilities and code speed, at the time of writing of this paper (November 2009) only 37% of the 1120 VIRTIS-M cubes acquired between June 2006 and July 2008 have been processed, providing nevertheless an extensive data set suitable for temperature profile studies. Processed data cover fairly uniformly the considered period, despite a strong variability in the available VIRTIS data volume during the mission (Figure 1). This processing work has resulted in more than $2.5 \cdot 10^5$ individual temperature profiles available for the present analysis.

3. Data Processing

[10] Prior to further processing, we removed from our data set individual retrievals derived from observations acquired either at emission angles greater than 30° or at sun-zenith angles lower than 95°. The former filter was applied to reduce the weight of temperature profiles affected by larger modeling uncertainty. The latter filter was applied to remove completely the effects of the scattering of solar photons. This radiation source has a non negligible effect on radiances measured at the center of the 4.3 μm band even when the Sun is few degrees below the horizon and adversely affects temperatures retrieved above 80 km. The two filters allowed more than 1.48×10^5 profiles to be available for further analysis.

[11] We classified individual temperature profiles on the basis of latitude and subsolar longitude at the time of acquisition (the latter quantity being equivalent to local time), in bins 2° × 2° (latitude-longitude) wide. The number of profiles inside each bin ranges from zero to almost 200 (Figure 2). Most VIRTIS-M observations have taken place in the vicinity of the Venus Express apocenter (almost above the South pole), to take advantage of the wider spatial coverage permitted by the greater distance. Extensive observations in the northern hemisphere have been performed by VIRTIS-M (by means of cubes at much smaller spatial coverage) and by VIRTIS-H (as stripes of spectra). Because of the very different spatial resolution, the processing of these observations has been postponed and will not be considered in this analysis.
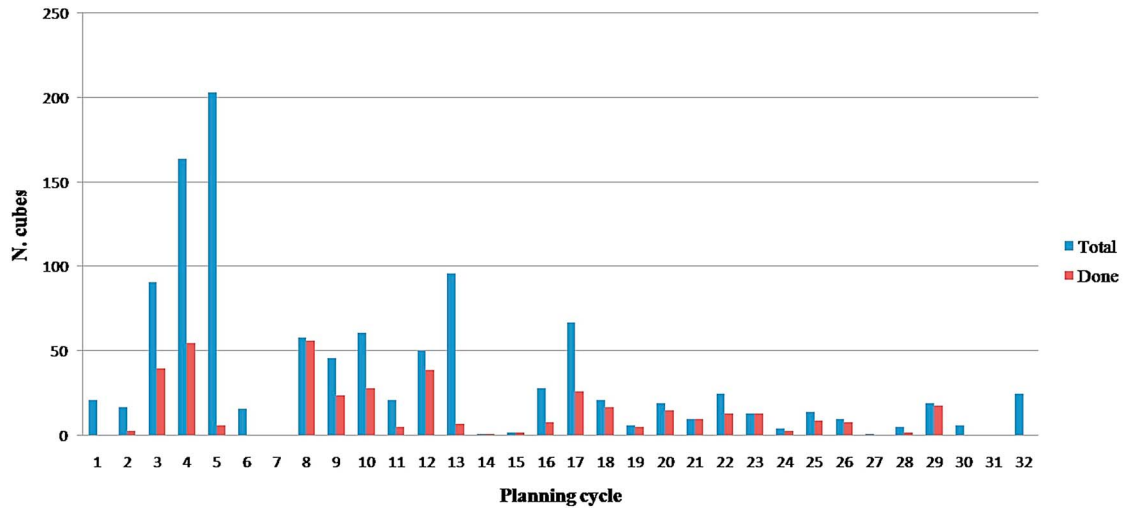
Temperature retrieval statistic

Figure 1. Statistics on the processing of VIRTIS-M data for the purpose of temperature retrieval. For each Medium Term Plan (MTP) cycle, corresponding to 4 weeks of operations, we compare the number of cubes that have been processed at the current date (Nov. 2009) to the total number of available cubes suitable for temperature analysis. This latter number does not include cubes acquired on the dayside or with exposure times optimized for the study of atmospheric windows in the near-infrared. MTP 2 covers the period June, 3rd – July, 1st 2006; MTP29 covers the period June, 28th – July 26th 2008.

[12] After binning, we considered individual bins one by one. For each given pressure level of the reference retrieval grid, the N individual profiles in the bin provided N independent estimates. This population was further processed in the three following steps.

[13] 1. We computed preliminary values of mean temperature T_0 and standard deviation σ_0.

[14] 2. We defined a sub-population considering the elements that lie within $2\sigma_0$ from T_0.

[15] 3. If we had at least 3 remaining elements in the sub-population defined in step 2, we used them to determine final values of mean temperature T_1 and standard deviation σ_1. If sub-population had two or less elements, the bin was not considered in subsequent analysis.

[16] Eventually, we obtained two three-dimensional matrices of air mean temperatures and standard deviations as function of latitude, local time and pressure. Step 2 listed above was required to filter the retrieval results driven mostly by the numerical instability that affects the relaxation inverse techniques. A comparison of standard deviation matrices obtained with and without step 2 demonstrated that - even if this step reduces the absolute values in the matrix of deviations - relative trends remain unchanged. The matrix of mean values is basically unaffected by the introduction of step 2, exception made for the bins with a small initial population (i.e.: northward of 40S) where a much smoother behavior is observed.

[17] Unstable retrievals are not associated to specific conditions or specific regions of Venus atmosphere. They are mostly related to residual calibration issues in the input data. These issues can occur more frequently in specific parts of VIRTIS focal plane (some clusters of pixels may show systematic shifts in the signal level) or can be randomly distributed (due to cosmic rays on the detector or spikes in the electronics) and eventually result in "unrealistic" Venus spectra. Namely, step 2 was introduced to deal with residual problems in the calibration pipeline and not to overcome weakness of the retrieval algorithms. The problematic cases are easily detected by visual inspection, but, at the current date, we were not yet able to implement a robust filter against anomalous data, suitable to pre-process the (literary) millions of individual VIRTIS-M spectra.

[18] The proper interpretation of the presented fields accounts for the different statistical weights of regions in the latitude-local time space. Regions with small retrieval populations in Figure 2. are naturally subjected to higher fluctuations. Moreover regions at the northern rim of the
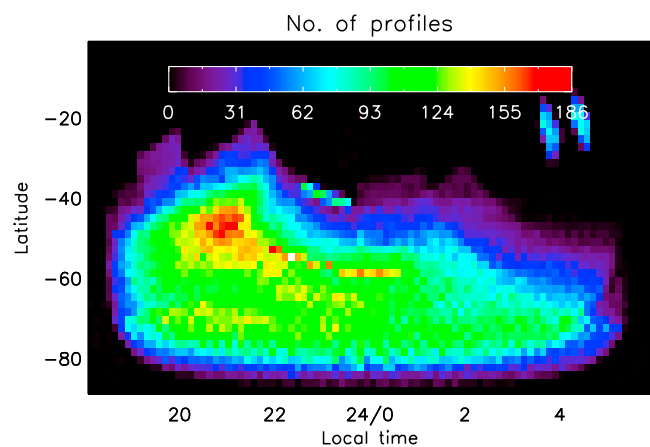

Figure 2. Coverage of VIRTIS-M temperature retrievals in the latitude – local time space. Color code gives the number of individual retrievals falling in each bin. Bin sizes are 2° × 2°.
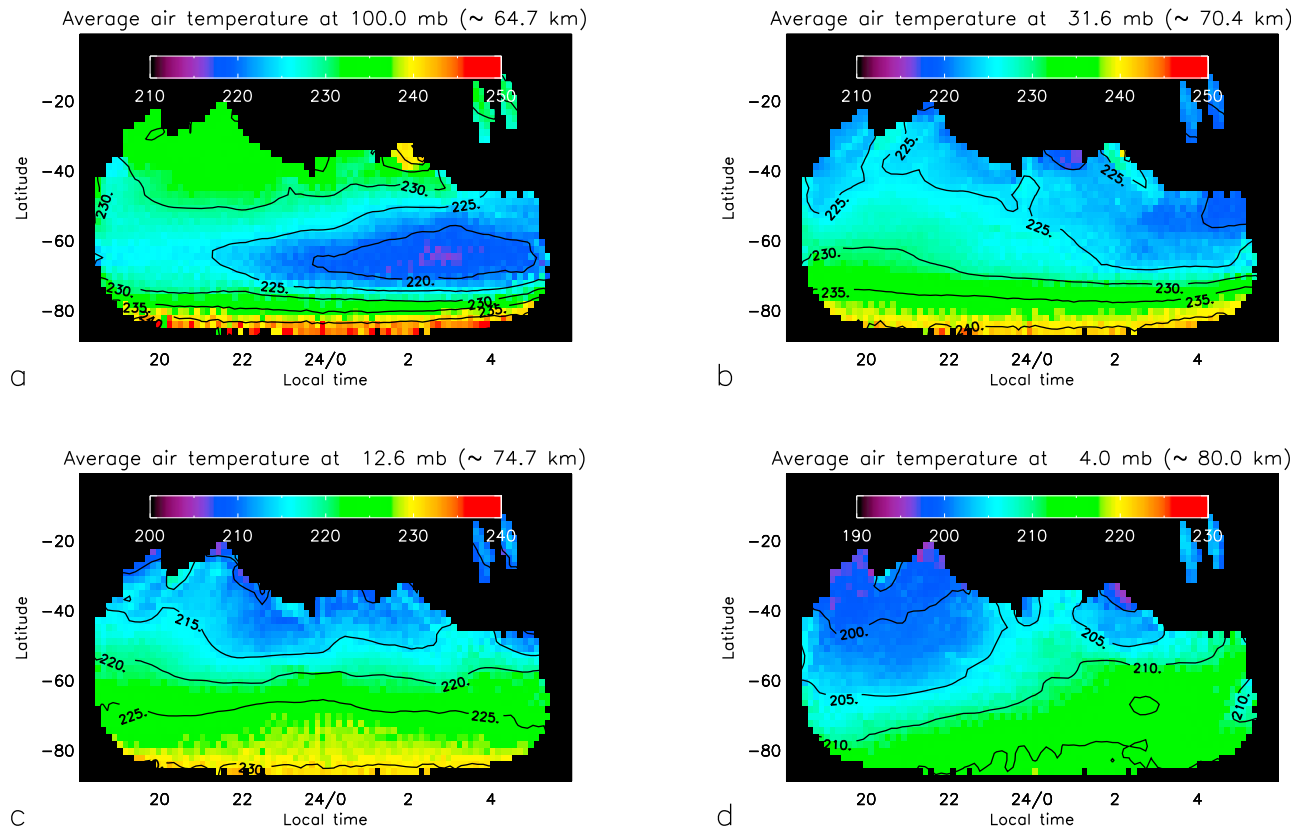
Figure 3. Mean temperature field as a function of latitude and local time for four selected pressure levels: (a) 100 mbar, (b) 31.6 mbar, (c) 12.6 mbar, (d) 4.0 mbar. A 3 × 3 smoothing on the sampling points of the original latitude/local time grid was applied before level curves were drawn to improve readability.

map are observed at higher emission angles and, despite the specific filter described above, relatively higher retrieval errors and related fluctuations can be expected. Finally, a filter on sun zenith angle excludes completely the measurements close to terminator (i.e.: at the lower and side boundaries of map in Figure 2), with an observed reduction in standard deviation compared to nearby regions.

[19] The averaging process extended over an entire population acquired at a fixed local time. This implies an assumption on the minor role played by possible seasonal trends in determining the atmospheric thermal structure. Even if this behavior is expected on the basis of the low values of Venus' orbital eccentricity and polar axis inclination, we performed nonetheless a quantitative analysis. This investigation confirmed that – for a given pressure level - data inside each bin do not present any systematic correlation with the Julian date of acquisition beyond the confidence levels set by random retrieval error and data dispersion.

[20] It shall be noted that the overall VIRTIS-M data processing contained two consecutive averaging processes. The first one involved the radiances (section 2), binned on the image plane. Resulting average radiances were used as input for temperature retrieval code. The second one involved the output temperatures, binned in latitude-local time bins from which the temperature is retrieved. This scheme has a twofold advantage with respect to averaging all radiances in latitude-local time bins and then perform the temperature retrieval. First, each average radiance derives

from the same number of input spectra, implying the same effective radiometric error and the same retrieval error for each derived temperature profile. Second, the scheme allowed different sizes of latitude-local time bins to be tested and allowed possible seasonal effects to be studied without having to repeat the time-consuming temperature retrieval.

[21] Tests on different bin sizes for the second average demonstrated that the results presented in this paper remain quantitatively the same. Namely, invariance of results varying the bin sizes was verified for different possible sections of the three-dimensional matrices of air mean temperatures and standard deviations: latitude/local time, latitude/pressure, latitude/pressure.

4. Results

[22] Mean and standard deviation matrices were used to produce horizontal maps at fixed pressure levels and vertical cross sections at fixed latitudes and fixed local times. Amplitudes of features observed in these maps can be compared against the retrieval error on individual profiles, as estimated by *Grassi et al.* [2008]: about 4K at 100 mbar and 1K between 70 and 2 mbar.

4.1. Latitude-Local Time Maps

[23] At the pressure level of 100 mbar (roughly corresponding to 65 km above reference surface) air temperatures on the evening side are usually warmer than on the morning side (Figure 3a), with differences well above the
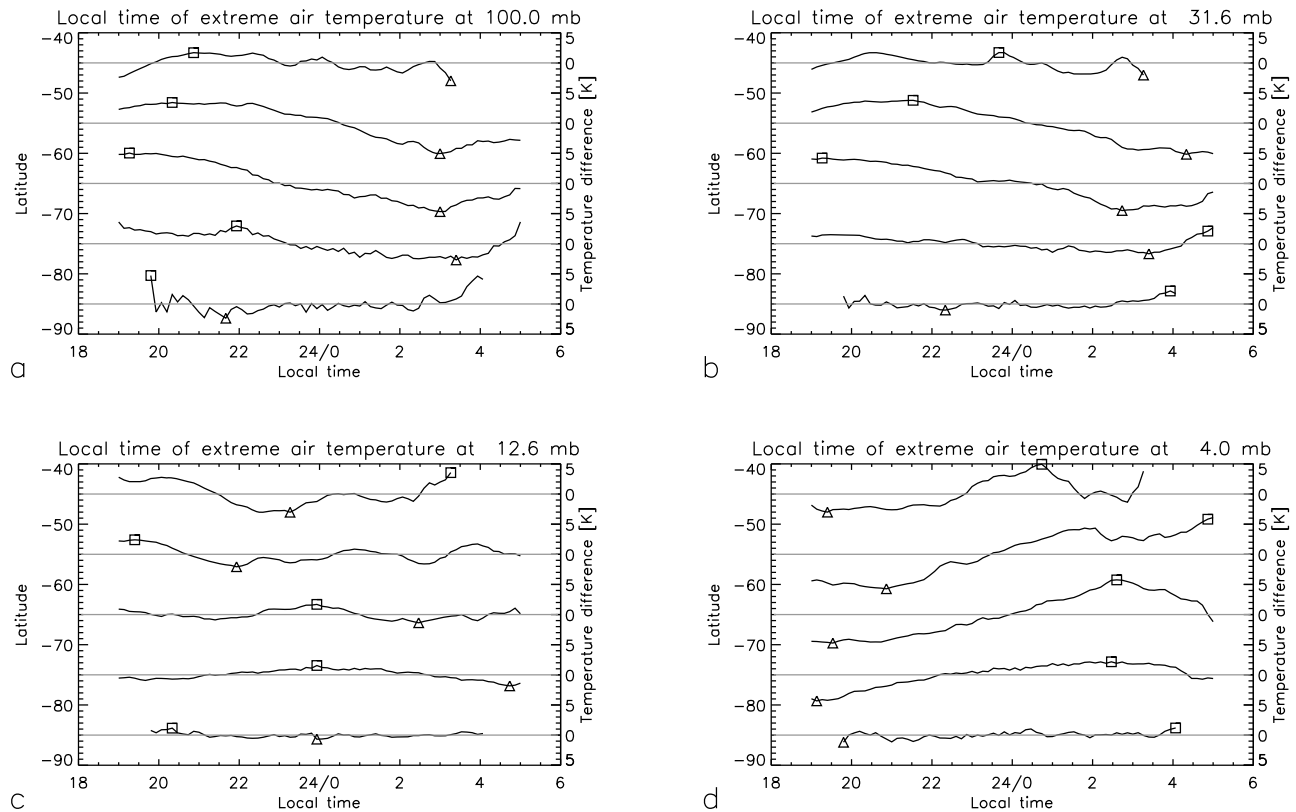
Figure 4. Air temperature versus local time for selected pressure levels and latitudes. Each plot refers to a fixed pressure level: (a) 100 mbar, (b) 31.6 mbar, (c) 12.6 mbar, (d) 4.0 mbar. In each plot, variations of air temperature around the mean value are presented for latitudes 85S, 75S, 65S, 55S, and 45S. Local times of maximum (squares) and minimum (triangles) air temperatures are also marked.

retrieval error level (Figure 4a). Namely, at any fixed latitude northward of 75S, a maximum is observed between 18.5LT and 22LT and a minimum between 1.5LT and 3.5LT. Temperatures southward of 75S are monotonically increasing with latitude toward the pole and have weak local time dependence. The 'cold collar' (first reported by *Taylor et al.* [1980]) is well evident in Figure 3a as the colder region centered around 65S. VIRTIS data show its local time structure, being the feature considerably colder (about 8K) on the morning side.

[24] The appearance of the thermal field changes quickly moving to the pressure level of 31.6 mbar (~70 km). The cold collar completely disappears and temperatures increase monotonically from 40S to southern pole at every local time (Figure 3b). A local maximum still exists at 20LT for latitudes between 40S and 70S, and the evening hemisphere remains the warmer one (Figure 4b).

[25] At the pressure level of 12.6 mbar (~75 km), the asymmetry between the morning and evening hemispheres almost entirely disappears (Figure 3c). In the region around 50S, two maxima are observed around 20LT and 4LT and a third one begins to develop around 1LT (Figure 4c). This local time maximum (slightly shifted around 0 LT) becomes the most relevant feature between 70S and 85S. Even if its amplitude lies close to retrieval error level, its extension in the latitude and local-time space suggests that we are dealing with a genuine feature of Venus atmosphere. Temperatures

remain monotonically increasing southward at every local time.

[26] At the pressure level of 4 mbar (~80 km), the morning hemisphere becomes the warmer one (Figure 3d). Northward of 75S, 20LT is the the colder time (Figure 4d), with evening-morning differences well above the retrieval error. For regions north of 60S, two local time maxima at 1LT and 4LT are observed, while southernmost temperatures appear more uniform. Again temperatures remain monotonically increasing toward the south at every local time.

[27] General features of thermal fields derived from visual inspection of Figure 3 are also evident in the summary of Venera 15 FTS data (covering the northern hemisphere) presented by *Zasova et al.* [2007]. Figures 6c and 6d of *Zasova et al.* [2007] show the cold collar region (65S and 100 mbar) being warmer on the evening side, while the atmosphere at higher altitudes toward the equator (namely, at 4 mbar and 50S) presents higher values of temperature toward the morning side.

[28] At the pressure level of 100 mbar, the standard deviation of the air temperatures appears particularly high in the latitudinal band around 80S (Figure 5a). Since (a) this region is where lobes of the polar vortex appear more frequently, (b) the lobes have clear counterparts in temperature fields at this pressure level [*Grassi et al.*, 2008], and (c) the lobes have an apparent rotation period of 4 days, we can
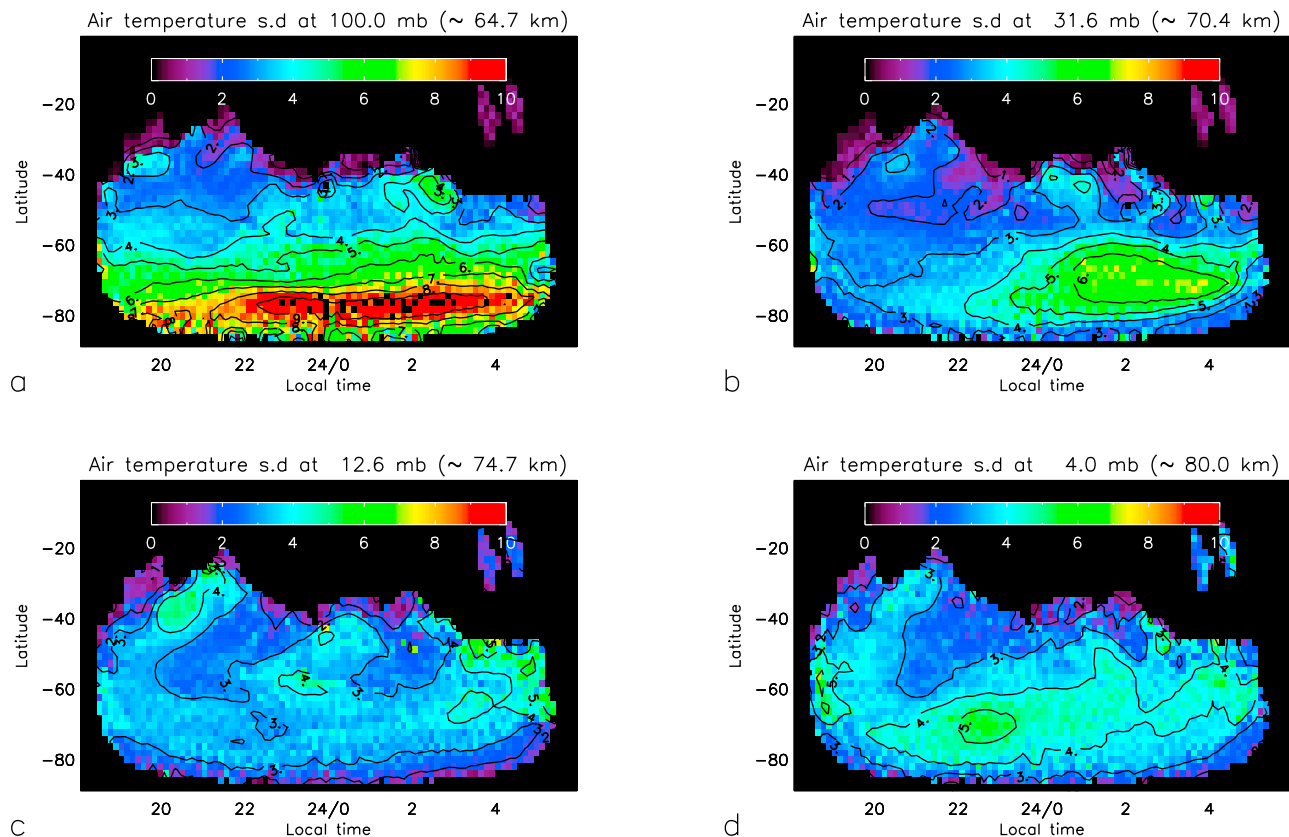
Figure 5. Temperature standard deviation field as a function of latitude and local time for four selected pressure levels: (a) 100 mbar, (b) 31.6 mbar, (c) 12.6 mbar, (d) 4.0 mbar. A 3 × 3 smoothing on the sampling points of the original latitude/local time grid was applied before level curves were drawn to improve readability.

expect that the polar vortex lobes induce a high variability in the temperature field exactly where we detect it. Latitudes northward of 60S (i.e.: outside the cold collar) show a lesser variability of temperatures.

[29] At 31.6 mbar, the standard deviation field is more asymmetric in local time, with the morning side southward of 50S showing more temperature variability (Figure 5b). Pressure levels around 12.6 mbar present a very low temperature variability for latitudes southward of 60S (Figure 5c). An increase possibly exists toward 4LT.

[30] Moving to the 4 mbar level, an increase of temperature standard deviation is observed with respect to the 12.6 level southward of 60S (Figure 5d) for almost all local times. This observation is consistent with the preliminary analysis derived from Figure 14 of *Grassi et al.* [2008], who observed a higher variability of temperature fields around 1mbar, especially evident on the morning side.

4.2. Local Time-Pressure Maps

[31] Further details of average fields can be appreciated in vertical cross sections along fixed latitudes. At 80S, the temperature field is remarkably symmetric around 24LT (Figure 6a). Temperature decreases monotonically with altitude from the 70 mbar level to 1 mbar. At 70 mbar, a slight decrease can be observed also moving toward lower altitudes. The average field presented here closely matches (with differences within 3K) results in Figure 14 of

Tellmann et al. [2009], including the two higher temperature lobes near 60 mbar at 18.5LT and 5.5LT, and the slight upward curvature of isothermal lines around 24LT.

[32] At 70S, the temperature field is strongly asymmetric in local time (Figure 6b). The evening side has an extended region of temperature inversion for a warm air slab centered around 40 mbar. Conversely, air temperatures are warmer on the morning side for altitudes above the 10 mbar pressure level. These two effects contribute to create steeper temperature gradients on the evening side for altitudes above the 40 mbar level. Moving further northward at 60S (Figure 6c), while temperatures remain higher on the morning side for higher altitudes, a local maximum around 24 LT develops for altitudes around the 10 mbar level.

[33] This maximum is also evident at 50S (Figure 6d), where it expands toward higher altitudes in the atmosphere. The simultaneous rise of isothermal levels toward the sunset terminator at 18.5 LT creates at about 5 mbar a series of three maxima of similar amplitude (with an irregular spacing of about 5 h). In the same map, we can see the development of a temperature maximum for altitudes below the 50 mbar level centered at 21LT. A similar map for 40S (not shown here) shows a further expansion in local time of this warm region.

[34] The standard deviation map at 80S presents a strong increase for altitudes below the 30 mbar level (Figure 7a). We also note an increase of standard deviation for altitudes
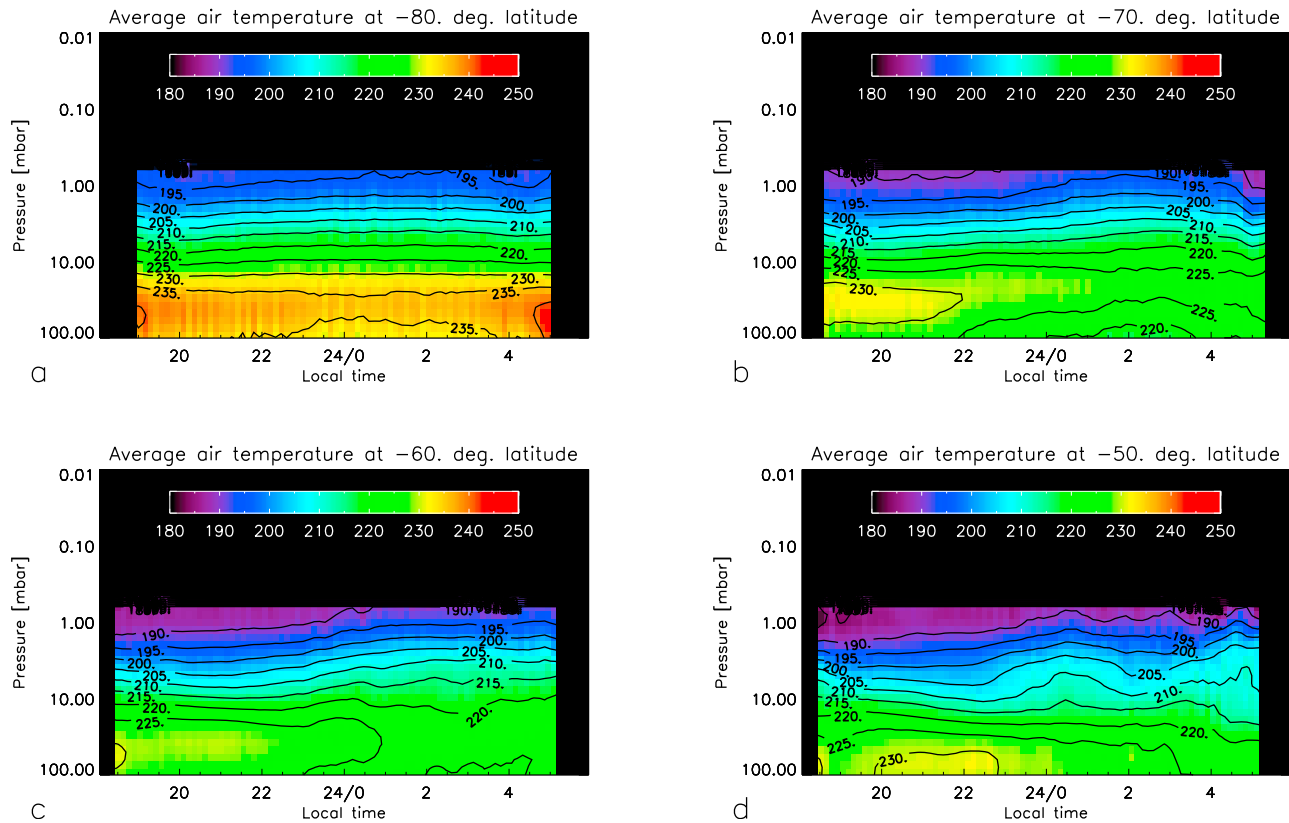
Figure 6. Mean temperature field as a function of local time and pressure for four selected latitudes: (a) −80°, (b) −70°, (c) −60°, (d) −50°.

higher than 10 mbar level, where a minimum value is observed. This region of minimum variability has an altitude not constant in local time, being lower around 21LT.

[35] Qualitatively similar trends are observed at 70S (Figure 7b). The pressure range of minimum standard deviation is now even more evident and clearly displaced toward higher altitudes in the morning hemisphere. For morning hours, an area of higher variability is also observed at altitudes below the 10 mbar level. For both maps in Figures 7a and 7b, the observed values of standard deviation (higher than the expected retrieval random error) and the clear local time trends (which rule out any possible effect due to the adopted pressure sampling grid) confirm that we are observing genuine features of Venusian atmosphere.

[36] Moving further northward, standard deviation fields become more fuzzy and ambiguous to interpret (Figures 7c–7d). An irregular region of minimum variability still exists for altitudes below the 10 mbar level, while a region of stronger variability centered at 0.5LT and for altitude higher than 3 mbar level appears more dubious.

4.3. Latitude-Pressure Maps

[37] Figure 8 presents average air temperature latitude-pressure maps at different local times. At 19 LT (Figure 8a) air temperatures increase from intermediate latitude toward the pole for all altitudes above the 30 mbar level. At lower altitudes, the temperature minimum related to cold collar at 65S and 100mbar has a moderate amplitude (T > 225K). A slab of warmer air (defined by the isothermal curve of 230K) overlays part of the cold collar, protruding directly from the polar region. Figure 8a can be compared with the Figure 11 of *Grassi et al.* [2008]. Differences are usually below 2K, with the average field northward of 75S systematically warmer at higher altitudes and colder at lower altitudes. Stronger discrepancies (<6K) are observed southward of 80S and for altitudes below the 30mbar level, and are consistent with the standard deviation values at 19LT shown in Figure 9a (see description below). The thermal field preserves its qualitative trends later in the evening (21LT, Figure 8b). However, we observe that air temperatures become warmer south of 50S, with the temperature increase more evident for altitudes above the 3 mbar level (185K isothermal curve disappears) and lower than 10 bars (development of a warmer region defined by the 230K isothermal).

[38] At 0LT (Figure 8c), the cold collar becomes more pronounced (temperature decreases below 225K near 60S near the 100 mbar level). In the region of transition between the cold collar and warmer polar regions, isothermal curves become almost vertical (e.g.: isothermal line at 230K). North of 55S and for altitudes below the 10 mbar level, air temperature become colder with respect to earlier local times, while a thermal increase is observed for altitudes higher than 3 mbar level. On the whole, the vertical thermal gradient is reduced for altitudes above the 10 mbar level and latitude north of 55S. In the late night (3LT, Figure 8d) the air temperature in the cold collar center reaches a minimum value below 220K. The temperature decrease extends to
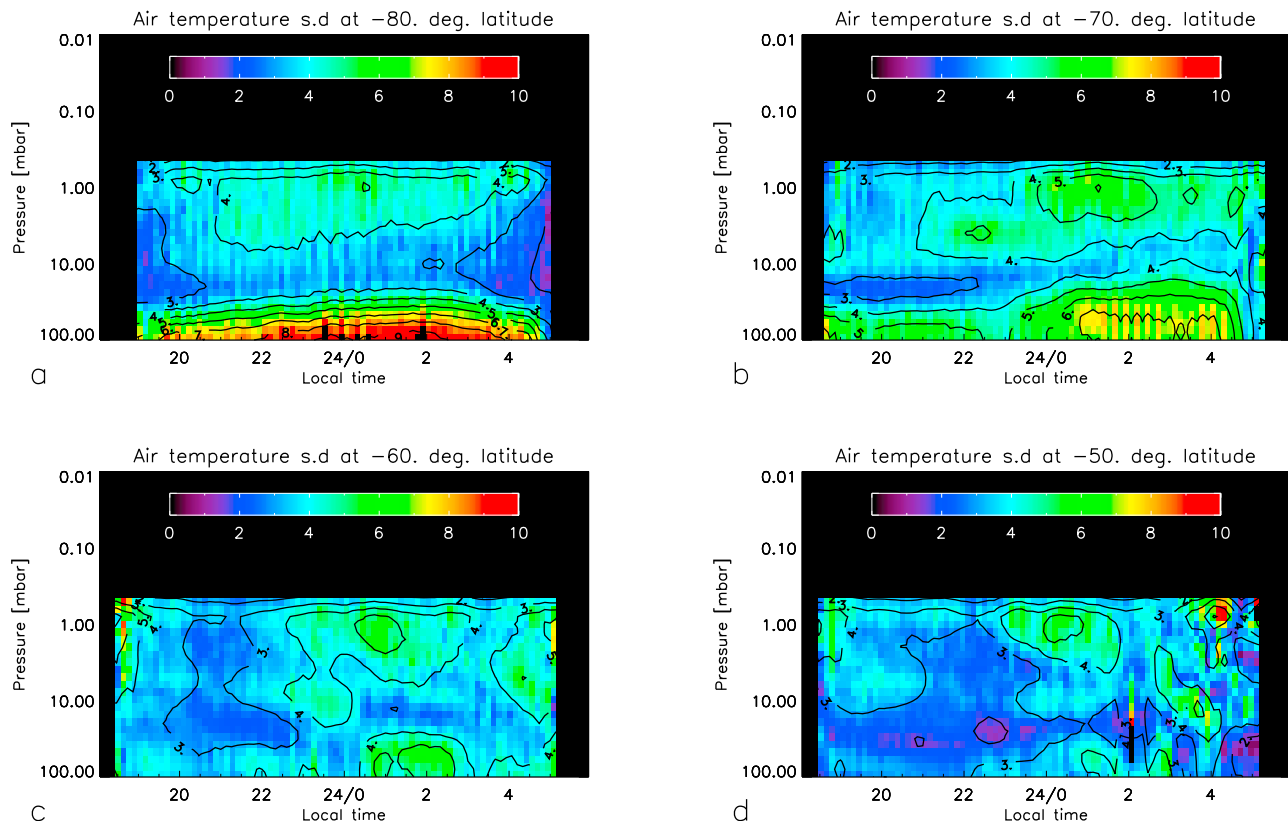
Figure 7. Temperature standard deviation field as a function of local time and pressure for four selected latitudes: (a) −80°, (b) −70°, (c) −60°, (d) −50°. A 5 × 5 smoothing on the sampling points of the original local time/pressure grid was applied before level curves were drawn to improve readability.

altitudes above the 10 mbar level northward of 75S, and is most evident around 55S.

[39] Figure 9 shows corresponding standard deviation maps. All four maps show that the regions affected by the polar dipole and cold collar (altitudes below the 30 mbar level, lat <60S) are subject to higher temperature variability. Standard deviation values increase with time along the night, while more variable region expands initially toward the south, and it only affects levels up to 10mb around 65S after 0LT.

[40] A second region of higher variability affects the region between 1 and 3 mbar around 70S. It is weaker at 19LT and reaches a maximum around midnight. The two regions are separated by a minimum standard deviation level ($\sigma < 4K$) that moves upward (from the 30 mbar level to 8 mbar) during the night.

[41] Standard deviation fields confirm the preliminary findings derived from Figure 14 of *Grassi et al.* [2008]: air temperature variability has a local maximum around 70S and pressures of few millibars and tends to increase during the night. Noteworthily, temperature variability in the lower atmosphere (100 mbar) southward of 60S is stronger in Figure 9 than in Figure 14 of *Grassi et al.* [2008]. It should be noted that Figure 14 of *Grassi et al.* [2008] was derived from the analysis of just seven VIRTIS-M data cubes acquired within 5 h. This fact suggests that variability in the lower atmosphere toward the pole is caused by phenomena (such as rotation of polar dipole) with time scales much

longer than few hours, while variability for altitudes above 10 mbar is caused by more rapid physical processes.

5. Discussion

[42] Absolute values of average temperature fields retrieved from VIRTIS-M and FTS [*Zasova et al.*, 2007] usually agree within 5K. This agreement is obtained despite the differences in the spectral range adopted for the retrieval and in the width of the weighting functions, both factors being optimal for the Soviet experiment. The agreement demonstrates therefore: a) the overall high quality of the absolute radiometric calibration for both instruments, b) the robustness of the retrieval algorithm, and c) the actual minor role played by the uncertainties in the aerosol vertical distribution in driving the temperature retrieval errors. The FTS spectral range covered the main H_2SO_4 cloud features and it was therefore possible to retrieve the cloud density and properly assess its effects in the analysis of individual spectra. The very similar results achieved by adopting a mean aerosol density profile in the analysis of VIRTIS spectra rule out the possibility that aerosol variations are a major source of systematic retrieval errors. Good correspondence (within 3K at 80S) with VeRA thermal fields [*Tellmann et al.*, 2009] further supports the idea that Figures 3 and 6 describe genuine variations in Venus air temperatures.

[43] The variety of features described in section 4 confirms the major role played by dynamics in driving the
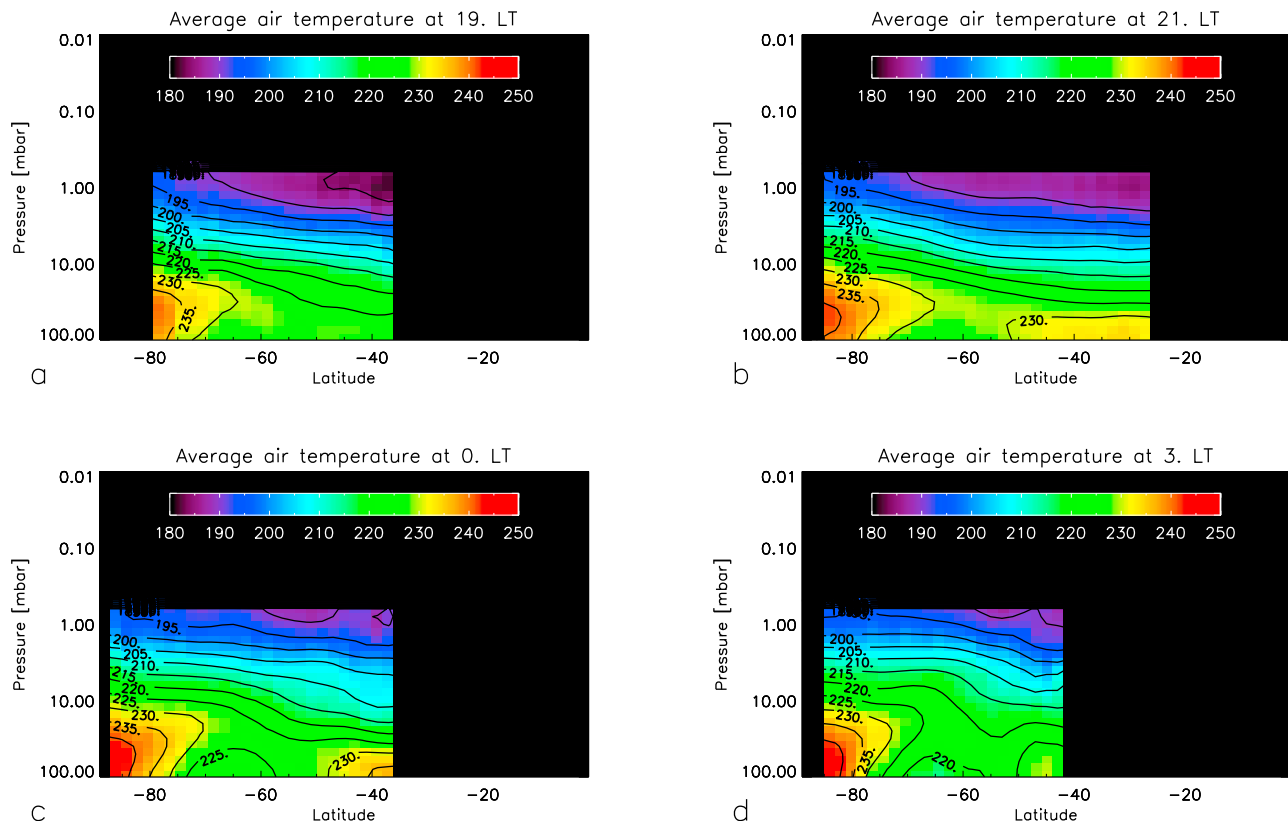
Figure 8. Mean temperature field as a function of latitude and pressure for four selected local times: (a) 19 LT, (b) 21 LT, (c) 0 LT, (d) 3 LT.

temperature fields in Venus' atmosphere between 65 and 90 km. A Hadley cell that extends throughout the entire northern (or southern) hemisphere has long been postulated as the main cause of temperature increase from midlatitudes to the pole [*Taylor et al.*, 1980].

[44] Patterns of temperature vs local time at 100 mbar (Figure 3a) are of particular interest. A series of plots similar to Figure 4a (not shown), but derived from orbit intervals corresponding to about 1/4 of a Venus synodic day, indicates that the location of the 100 mbar, 65S minimum does not change significantly in local time, with possible extreme variations between 1 and 3LT. The maximum/minimum pattern appears consistent with a sun-synchronous wave with a semi-amplitude of 4K and a wavelength of approximately 180° longitude (maximum and minimum are about 100° longitude apart, see Figure 4a, central plot). The observations by VIRTIS are consistent with the effects of a semidiurnal component of the thermal tide, particularly strong in the region of the southern cold collar (100 mb, 65S). Actually, thermal tides in Venus' mesosphere have been recognized in their wave number-2 component in OIR [*Schofield and Taylor*, 1983], FTS [*Zasova et al.*, 2007] and VeRa [*Tellmann et al.*, 2009] data. Noteworthily, both OIR and FTS observed mostly the northern hemisphere.

[45] Moving to higher altitudes, we can observe changes in the amplitude ΔT and phase of the thermal wave (Figures 4b–4d). In the latitude range covered by our data, ΔT is minimal at 12.6 mbar. For any given latitude northward of 80S, the time of minimum temperature shifts from the morning to the evening side while moving from the

100 mbar to the 4 mbar level. The altitude-phase relationship confirms the previous findings derived from OIR data within 45° of the equator. Trends of wave number-2 ΔT as a function of altitude and latitude are described in Figure 8b of *Zasova et al.* [2007]. These authors report a level of minimum ΔT centered around the 31 mbar level, i.e.: about 5 km below the region of minimum ΔT (12.6 mbar) derived from VIRTIS data. The *Zasova et al.* [2007] plot describes, for altitudes above the 31 mbar level, a steady increase of ΔT moving from 55S (ΔT about 1.5K at 4 mbar) toward the equator. Even if VIRTIS data present a qualitatively similar trend, ΔT is already on the order of 5K at 55S and 4 mbar. The relative amplitudes of the different components of the thermal tides and other significant atmospheric waves have been recently investigated by *Lebonnois et al.* [2010] and *Lee et al.* [2007] using Venus atmospheric global circulation models (GCMs).

[46] The GCM model by *Lebonnois et al.* [2010] (which incorporates a detailed treatment of radiative transfer processes) shows a strong wave component at 70S and 65km-altitude, related to a wave number-1, quasi-bidiurnal wave. While the amplitude of this wave (10K) is comparable to the temperature differences between maximum and minimum at 70S observed in VIRTIS-M field (Figure 3a), such a quasi-bidiurnal wave should be migrating in the local time coordinate system. Such a migrating character is apparently not detected in our data, nor does the maximum/minimum pattern in the nightside seem compatible with a wave number-1 wave. In the Lebonnois *et al.* results, the altitudes toward 80km show increasing wave amplitudes toward the equator
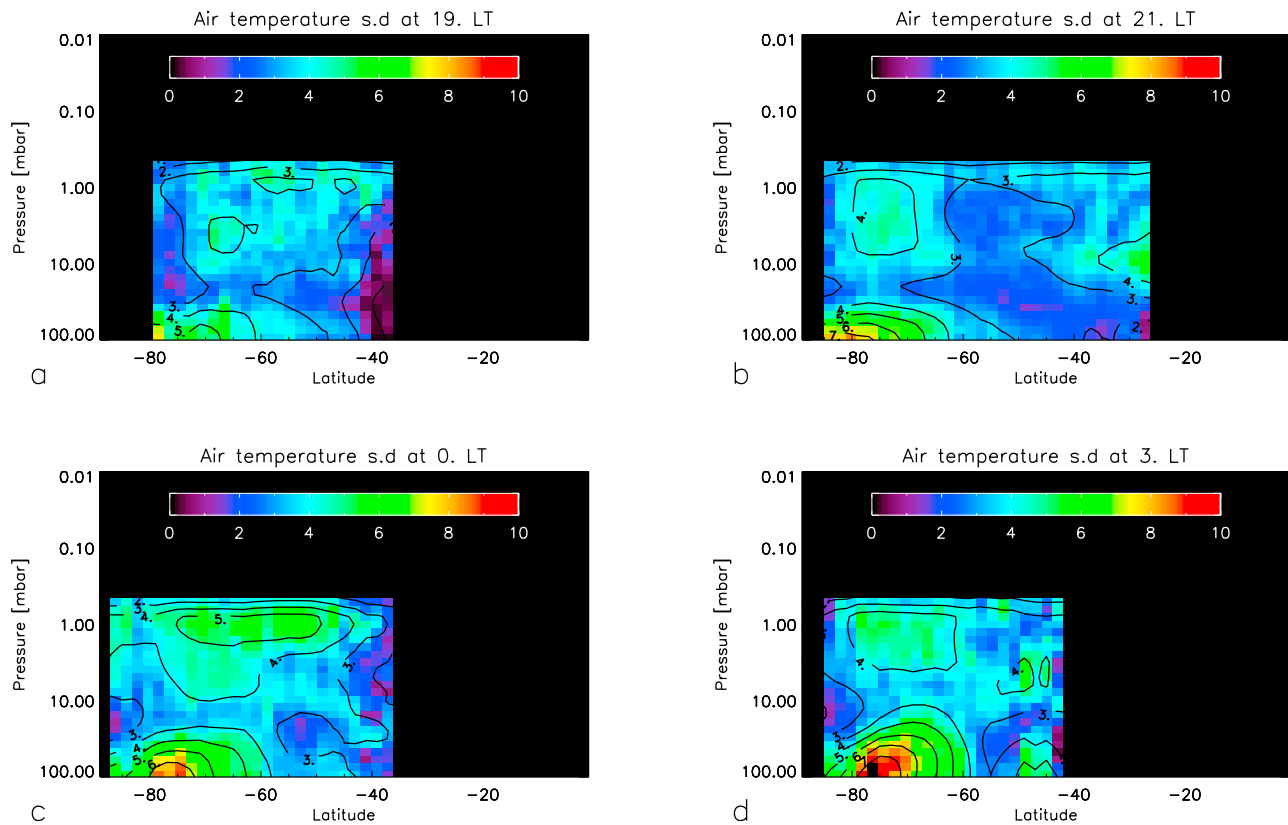
Figure 9. Temperature standard deviation field as a function of latitude and pressure for four selected local times: (a) 19 LT, (b) 21 LT, (c) 0 LT, (d) 3 LT A smoothing of 5 × 5 on the sampling points of the original latitude/pressure grid was applied before level curves were drawn to improve readability.

(mostly due to semidiurnal tides), as confirmed by VIRTIS data analysis. Nevertheless, the amplitude of the waves in the model (about 2K) remains smaller than the temperature differences at 50S observed in the VIRTIS-M field of Figure 3d.

[47] The GCM model by Lee *et al.* predicts an amplitude peak for the wave number-2, semidiurnal component of the thermal tides around 100 mbar for the 65S latitude region. Even if the expected amplitude (about 2K) is much smaller than the temperature differences around the same latitude observed in VIRTIS-M field of Figure 3a, the qualitative agreement supports the interpretation of the wave observed by VIRTIS as the semidiurnal component of the thermal tides.

[48] It is worth mentioning here that the main difference between the two GCMs is that the model by Lebonnois *et al.* makes use of a full radiative transfer code to calculate heating rates at each level of the atmosphere, whereas the model by Lee *et al.* uses a diurnally varying Newtonian cooling forcing, although it is able to well represent the main characteristics of Venus' atmospheric circulation, such as the superrotation and the midlatitude jets. On the other hand, the model of Lebonnois *et al.* may still suffer from disequilibrium between the vertical transport of angular momentum at the equator and the meridional transport of angular momentum toward the poles, which could translate into a biased representation of the relative amplitudes of the thermal tides at different latitudes. VIRTIS observations,

therefore, may prove extremely important to help constrain models of Venus' atmospheric circulation.

6. Conclusions and Future Work

[49] Preliminary analysis of the air temperature fields derived so far from VIRTIS-M has allowed us to derive a 3D map of the average thermal field of the southern Venus mesosphere, suitable for statistical analysis. Several features of this field suggest the presence of thermal tides of wave number-2 (semidiurnal component). Despite the fact that a complete analysis in the spectral space remains beyond the purpose of this paper, several trends previously observed in OIR and FTS data sets find here a further confirmation in the VIRTIS observations of the southern hemisphere. Qualitative comparisons between data and GCM predictions show that some features of the observed thermal field variability are detectable in model results, but a more refined and quantitative approach is still required to obtain an appropriate description of sun-synchronous tides in the Venusian mesosphere.

[50] VIRTIS-M cubes still to be processed may allow us to develop, in the near future, a data set suitable for a complete Fourier analysis, should the daytime non-LTE contamination be modeled. Moreover, the extension of the methodology to VIRTIS-H data will allow us to achieve a good coverage of equatorial and northern latitudes and a

reference experimental benchmark for extensive validation of global circulation models.

References

Bertaux, J.-L., et al. (2007), SPICAV on Venus Express: Three spectrometers to study the global structure and composition of the Venus atmosphere, *Planet. Space Sci.*, *55*, 1673–1700, doi:10.1016/j.pss.2007.01.016.

Drossart, P., et al. (2007), Scientific goals for the observation of Venus by VIRTIS on ESA/Venus express mission, *Planet. Space Sci.*, *55*, 1653–1672, doi:10.1016/j.pss.2007.01.003.

Grassi, D., P. Drossart, G. Piccioni, N. I. Ignatiev, L. V. Zasova, A. Adriani, M. L. Moriconi, P. G. J. Irwin, A. Negrão, and A. Migliorini (2008), Retrieval of air temperature profiles in the Venusian mesosphere from VIRTIS-M data: Description and validation of algorithms, *J. Geophys. Res.*, *113*, E00B09, doi:10.1029/2008JE003075, [printed 114(E9), 2009].

Jenkins, J. M., P. G. Steffes, D. P. Hinson, J. D. Twicken, and G. L. Tyler (1994), Radio occultation studies of the Venus atmosphere with the Magellan spacecraft. 2: Results from the October 1991 experiments, *Icarus*, *110*, 79–94, doi:10.1006/icar.1994.1108.

Kliore, A. J. (1985), Recent results on the Venus atmosphere from Pioneer Venus radio occultations, *Adv. Space Res.*, *5*(9), 41–49, doi:10.1016/0273-1177(85)90269-8.

Lebonnois, S., F. Hourdin, V. Eymet, A. Crespin, R. Fournier, and F. Forget (2010), Superrotation of Venus' atmosphere analyzed with a full global circulation model, *J. Geophys. Res.*, *115*, E06006, doi:10.1029/2009JE003458.

Lee, C., S. R. Lewis, and P. L. Read (2007), Superrotation in a Venus general circulation model, *J. Geophys. Res.*, *112*, E04S11, doi:10.1029/2006JE002874.

Piccioni, G., et al. (2007), The Visible and Infrared Thermal Imaging Spectrometer, *ESA SP*, 1295.

Schofield, J. T., and F. W. Taylor (1983), Measurements of the mean, solar-fixed temperature and cloud structure of the middle atmosphere of Venus, *Q. J. R. Meteorol. Soc.*, *109*, 57–80, doi:10.1002/qj.49710945904.

Seiff, A. (1983), Thermal structure of the atmosphere of Venus, in *Venus*, edited by D. M. Hunten et al., pp. 215–279, Univ. of Ariz. Press, Tucson.

Taylor, F. W., et al. (1980), Structure and meteorology of the middle atmosphere of Venus Infrared remote sensing from the Pioneer orbiter, *J. Geophys. Res.*, *85*, 7963–8006, doi:10.1029/JA085iA13p07963.

Tellmann, S., M. Pätzold, B. Häusler, M. K. Bird, and G. L. Tyler (2009), Structure of the Venus neutral atmosphere as observed by the Radio Science experiment VeRa on Venus Express, *J. Geophys. Res.*, *114*, E00B36, doi:10.1029/2008JE003204.

Titov, D. V., et al. (2009), Venus Express: Highlights of the nominal mission, *Sol. Syst. Res.*, *43*, 185–209, doi:10.1134/S0038094609030010.

Yakovlev, O. I., S. S. Matiugov, and V. N. Gubenko (1991), Venera-15 and -16 middle atmosphere profiles from radio occultations: Polar and near-polar atmosphere of Venus, *Icarus*, *94*, 493–510, doi:10.1016/0019-1035(91)90243-M.

Zasova, L. V., N. I. Ignatiev, I. A. Khatountsev, and V. Linkin (2007), Structure of the Venus atmosphere, *Planet. Space Sci.*, *55*, 1712–1728, doi:10.1016/j.pss.2007.01.011.

A. Cardesìn-Moinelo, ESA, INSA, ESAC, PO Box 78, Villanueva de la Cañada E-28691, Spain.

P. Drossart, LESIA, Observatoire de Paris, 5 place Jules Janssen, F-92195 Meudon CEDEX, France.

D. Grassi, IFSI, INAF, Area di Ricerca Roma II, Tor Vergata, Via del Fosso del Cavaliere, I-00133 Roma, Italy. (Davide.Grassi@ifsi-roma.inaf.it)

S. Lebonnois and L. Montabone, Laboratoire de Météorologie Dynamique, IPSL, Université Pierre et Marie Curie, CNRS, Tour 45-55, BP 99, 4 place Jussieu, F-75252 Paris CEDEX 05, France.

A. Migliorini and G. Piccioni, IASF, INAF, Area di Ricerca Roma II, Tor Vergata, Via del Fosso del Cavaliere, I-00133 Roma, Italy.

L. V. Zasova, IKI RAS, 117997, 84/32 Profsoyuznaya Str., Moscow, Russia.